

## EMT-induced cell mechanical changes enhance mitotic rounding strength

Kamran Hosseini<sup>1</sup>, Anna Taubenberger<sup>1</sup>, Carsten Werner<sup>2</sup>, Elisabeth Fischer-Friedrich<sup>1,\*</sup>

<sup>1</sup> Biotechnology Center, Technische Universität Dresden, Tatzberg 47-49, 01307 Dresden, Germany

<sup>2</sup> Leibniz Institute of Polymer Research Dresden, Max Bergmann Center, Hohe Str. 6, 01069 Dresden, Germany

\* Corresponding author

Correspondence to: Elisabeth Fischer-Friedrich, Biotechnology Center, Technische Universität Dresden, Mailto: elisabeth.fischer-friedrich@tu-dresden.de. Phone: ++49 351 463 40235. Fax: ++49 351 463 40342.

### Abstract:

To undergo mitosis successfully, animal cells need to acquire a round shape to provide space for the mitotic spindle. The mitotic cell achieves this by deforming the surrounding tissue, a process which is driven by forces emanating from actomyosin contractility. Cancer cells are able to undergo cell division in mechanically challenging environments such as the increasingly crowded environment of a growing tumor suggesting an enhanced ability of mitotic rounding in cancer. Here, we show that epithelial mesenchymal transition (EMT), a hallmark of cancer progression and metastasis, increases mitotic rounding strength and thus promotes the ability of post-EMT cancer cells to reliably round up in mitosis. In addition, we show that the stiffness and contractility of interphase cells is reduced through EMT, suggesting that mitotic rounding is further promoted by reduced mechanical resistance of neighboring interphase cells. We report evidence that cell-mechanical changes upon EMT may be accounted for by an EMT-induced rise in activity of Rac1, which causes reduced contractility and cytoskeletal stiffness in interphase, while it leads to the opposite cell-mechanical phenotype in mitosis. We thus unveil a new mechanism of enhanced mitotic cell rounding through EMT suggesting an EMT-associated improved ability for cell division in the confined environment of a tumor.

## 1 Introduction

Most animal cells approach an approximately spherical shape when entering mitosis<sup>1</sup>. This process has been termed mitotic rounding. It ensures the correct morphogenesis of the mitotic spindle and, in turn, successful cell division<sup>2–5</sup>. When cells acquire a round shape at the entry of mitosis, they need to mechanically deform the surrounding tissue to do so (Figure 1). Previous studies suggest that the forces necessary for this deformation emerge from the contractility of the mitotic actomyosin cytoskeleton<sup>1,3,5–11</sup>. In fact, at the onset of mitosis, cortical contractility was found to be upregulated giving rise to an increased cell surface tension which drives the mitotic cell into a spherical shape<sup>8,9</sup>. This physical picture is consistent with reports that mitotic rounding relies on RhoA<sup>7,12,13</sup> – a major actomyosin regulator in the cell. In a growing tumor, an increasing cell density generates a compressive mechanical stress which would likely lead to an increasing mechanical obstacle for mitotic rounding. Indeed, mechanical confinement or external pressure have been shown to hamper cell proliferation in tumor spheroids<sup>14–18</sup>. Thus, it has been hypothesized that the actin cortex of cancer cells exhibits oncogenic adaptations that allow for ongoing mitotic rounding and division inside tumors<sup>19</sup>. In fact, it was shown that the human oncogene Ect2 contributes to mitotic rounding through RhoA activation<sup>7,10</sup> and that Ras overexpression promotes mitotic rounding<sup>20</sup>.

Epithelial-mesenchymal transition (EMT) is a cellular transformation in which epithelial cells loose epithelial polarity and intercellular adhesiveness gaining migratory potential<sup>21–23</sup>. EMT, a hallmark in cancer progression, is commonly linked to early steps in metastasis promoting cancer cell invasiveness. Moreover, EMT was connected to cancer stem cells and the outgrowth of secondary tumors<sup>21–23</sup>, suggesting that EMT may also be important for cell proliferation in a tumor.

Here, we study the influence of EMT on mitotic rounding strength by quantifying the mechanics, the contractility and activity of upstream regulators of the actin cortex in breast epithelial cells. For this purpose, we use an established dynamic cell confinement assay based on atomic force microscopy<sup>9,24</sup>. We report striking cell-mechanical changes upon EMT that are accompanied by a strong change in the activity of the actomyosin master regulators Rac1 and RhoA. Through measurements on knockdown cells, we identify Rac1 as a key regulator for a cell-cycle-dependent cell-mechanical switch that can account for EMT-induced changes. Furthermore, we give evidence that EMT induces actual changes in mitotic rounding in tumor spheroids embedded in mechanically confining, covalently crosslinked hydrogels<sup>25</sup>.

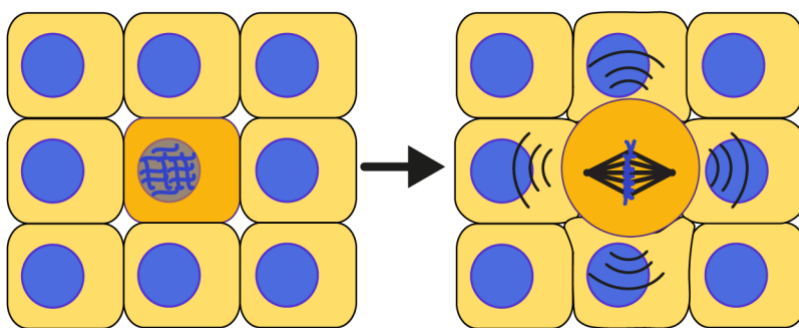


*Figure 1: Schematic of mitotic rounding in a tissue: At the onset of mitosis, cells need to deform their surrounding when acquiring a spherical shape in mitosis. Mechanical forces for rounding emerge, at least partly, from actomyosin contractility of the mitotic cell cortex.*

## 2 Results

### 2.1 Breast epithelial cells undergo EMT upon drug treatment

MCF-10A and MCF-7 are human breast epithelial cell lines. While MCF-10A are pre-neoplastic cells which serve as a model for mammary epithelial cells in healthy conditions, MCF-7 are cancerous cells derived from a metastatic mammary carcinoma but with an epithelial phenotype in regular growth medium.

We induce EMT in MCF-7 and MCF-10A breast epithelial cells respectively through established methods by incubation with phorbol ester (TPA)<sup>26</sup> or TGF- $\beta$ 1<sup>27-29</sup>, respectively (Figure 2, Materials and Methods). Accordingly, both cell lines showed a loss of the epithelial marker E-cadherin and an increase in mesenchymal markers Vimentin and N-Cadherin after treatment according to western blot quantification (Figure 2b and Figure S2).

Upon induced EMT, MCF-7 and MCF-10A cells underwent a phenotypical change: while untreated MCF-7 cells grew in clusters, modMCF-7 cells tended to grow isolated from each other and acquired a more spindle-shaped phenotype (Figure 2a). Furthermore, previous studies showed that TPA-treatment enhances proliferation and migration in MCF-7 cells corresponding to a more aggressive cancer cell phenotype<sup>26</sup>. In the case of MCF-10A, TGF- $\beta$ 1-treated cells also show a more spindle-shaped phenotype after EMT induction, but cell contacts are maintained. In addition, TGF- $\beta$ 1-induced transformation of MCF-10A was shown to enhance cell migration<sup>30</sup> but to inhibit cell proliferation – an effect reversed by oncogenic signaling<sup>31</sup>.

In the following, cells that underwent EMT will be denoted as modMCF-7 and modMCF-10A.

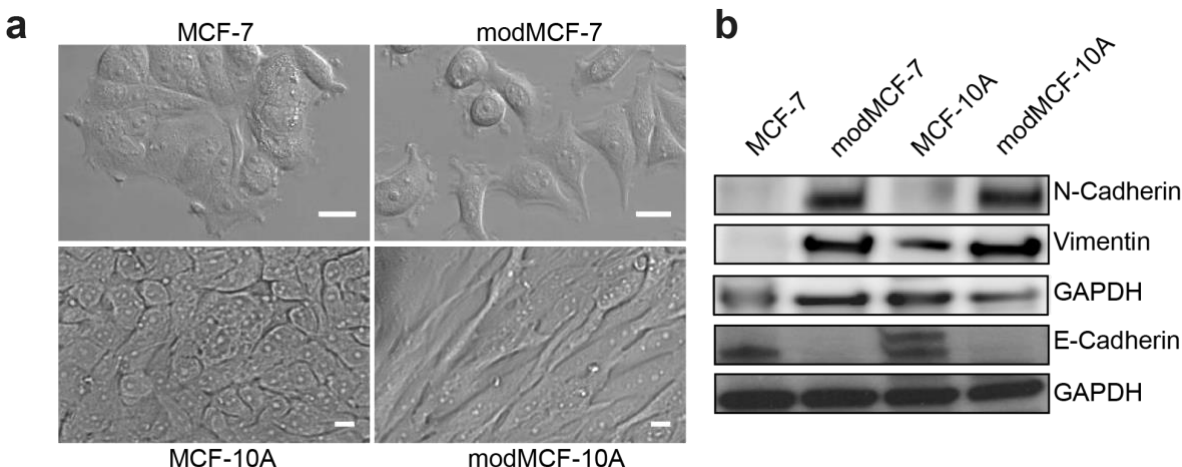


*Figure 2: Pharmacological induction of EMT in MCF-7 and MCF-10A cells through TPA and TGF- $\beta$ 1, respectively. a) Cell morphological changes upon EMT in MCF-7 (top row) and MCF-10A (bottom row). Scale bar: 10  $\mu$ m, both. b) Protein expression changes upon EMT: western blots of E-cadherin (epithelial marker), N-cadherin and Vimentin (mesenchymal markers) from cell lysates before and after EMT. Post-EMT cells are referred to as modMCF-7 and mod-MCF-10A, respectively.*

### 2.2 EMT induces a cell-cycle dependent cell-mechanical switch

We probed mitotic and suspended interphase cells mechanically before and after EMT through atomic force microscopy (AFM). We used a previously established cell confinement setup where initially round cells are moderately confined between two parallel plates using a wedged cantilever<sup>32-35</sup> (Figure 3a,b, Materials and Methods). This method was previously shown to measure the contractility and the viscoelastic stiffness of the actin cortex<sup>33,34</sup>. During measurements, we confined cells first to the desired confinement height and then imposed small cell height oscillations at a frequency of f=1 Hz (Figure 3c). Height oscillations result in an oscillatory force response of the cell cortex from which we extracted active cortical tension and a complex elastic modulus characterizing cortex mechanics at the chosen oscillation

frequency<sup>34</sup> (Figure 3c,d, Materials and Methods). In the following, we will refer to the absolute value of the complex elastic modulus as cortical stiffness. The complex phase of this modulus will be referred to as phase shift. This phase shift indicates the nature of the cortex material: a phase shift of 0 degree corresponds to a solid material, a phase shift of 90 degrees corresponds to a liquid material, while values in between indicate an intermediate viscoelastic behavior<sup>34</sup>. We thereby obtain three mechanical parameters of the cortex from the measurement of each cell: cortical stiffness, phase shift and cortical tension. These three parameters provide a detailed mechanical fingerprint of the cortical architecture of the cell.

First, we performed the cell confinement assay on interphase cells in suspension before and after EMT induction. The results show a striking decrease in cortical tension and stiffness following EMT induction (Figure 3e,g, upper row). In addition, we find that the phase shift of cortex mechanics increased in MCF-10A through EMT but did not change significantly in MCF-7 (Fig. 3f, upper row).

Secondly, we examined the mechanical properties of the cell cortex in mitotic cells before and after EMT. For measurements, cells were pharmacologically arrested in mitosis by addition of S-trityl-L-cysteine to enrich mitotic cells and prevent cell-cycle related mechanical changes (see Materials and Methods). To our surprise, we now observed the opposite cell-mechanical change after EMT (Fig. 3e-g, lower row); cortical tensions and cortical stiffness were clearly increased in both cell lines while phase shifts went down. In summary, our measurements show that the post-EMT mitotic cortex is stiffer, more contractile and more solid-like.

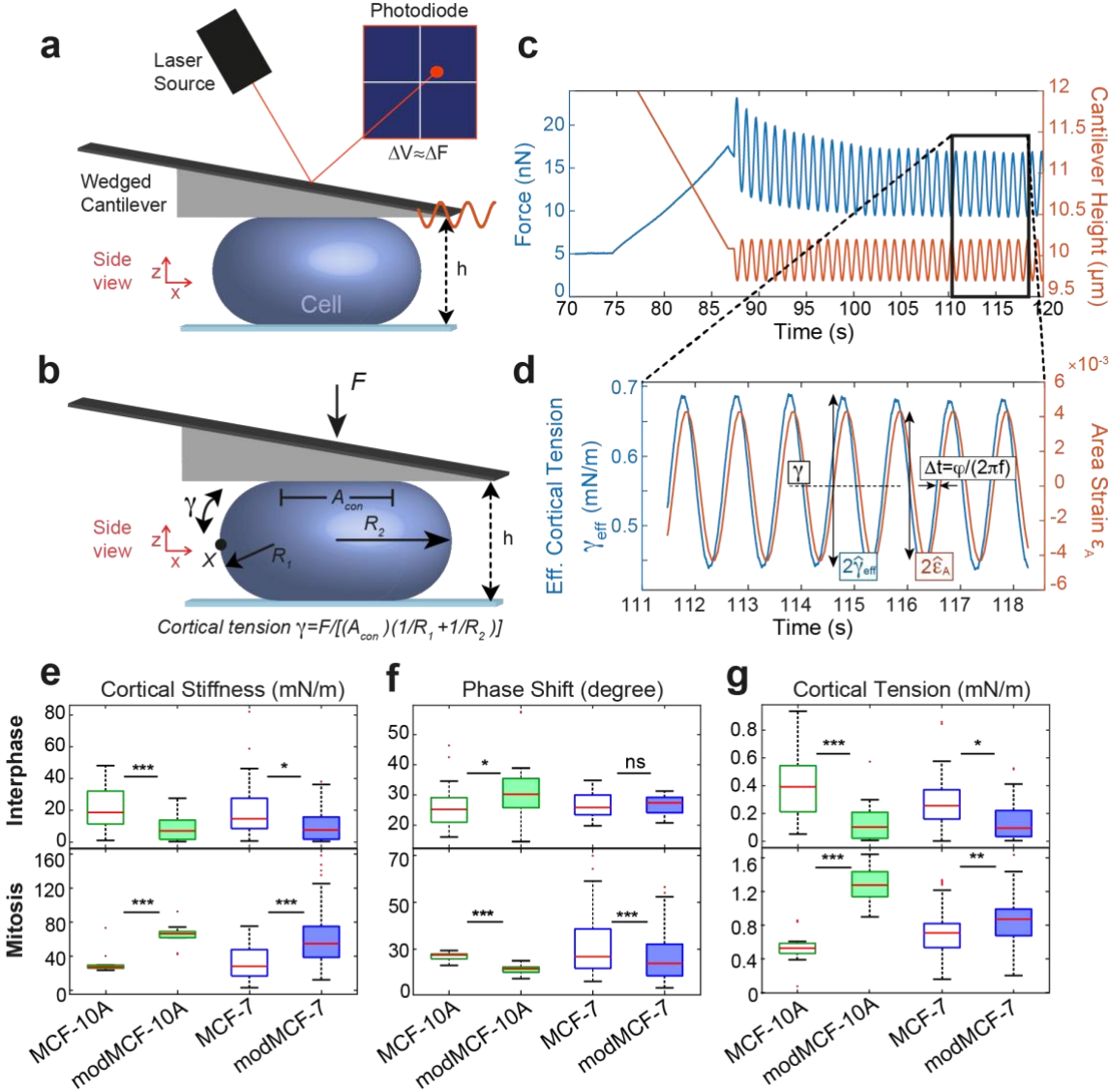


**Figure 3: Mechanical phenotyping of the actin cortex of MCF-7 and MCF-10A before and after EMT measured by dynamic AFM cell confinement. a) Schematic of measurement setup: initially round cells are confined by the tip of a wedged AFM cantilever and oscillatory height oscillations are imposed. b) Mechanical and geometrical parameters of a measured cell used for data analysis. c) Exemplary AFM readout during cell confinement and subsequent oscillatory cell height modulation: force (blue), cantilever height (orange). d) Effective time-dependent cortical tension estimate (blue) and relative cell surface area change (orange) from data analysis of the indicated time window in c. Mechanical parameters are determined as follows: **cortex stiffness**  $K$  is calculated as  $\hat{\gamma}_{\text{eff}}/\hat{\epsilon}_A$ , **phase shift** is obtained as  $\varphi = (2\pi f)\Delta t$ , **cortical tension** is calculated as time average of  $\gamma_{\text{eff}}$  (dashed black line). The corresponding complex elastic modulus of the cortex is  $K^* = K e^{i\varphi}$ . e-g) Cortical stiffness (e), phase shift (f) and cortical tension (g) measured for suspended interphase cells (top row) and cells in mitotic arrest (bottom row) before and after EMT. (Post-EMT cells are referred to as modMCF-7 and mod-MCF-10A, respectively. Number of cells measured: Interphase: MCF-7  $n=27$ , modMCF-7  $n=28$ , MCF-10A  $n=27$ , modMCF-10A  $n=31$ , Mitosis: MCF-7  $n=34$ , modMCF-7  $n=45$ , MCF-10A  $n=12$ , modMCF-10A  $n=12$ .  ${}^{ns}p > 0.05$ ,  $*p < 0.05$ ,  $**p < 0.01$ ,  $***p < 0.001$ ).**

### 2.3 EMT upregulates activity of Rac1 and downregulates activity of RhoA

We were interested in the molecular origin of the observed mechanical changes of the cortex. Since Rho-GTPases are known to be key regulators of the actin cortex, we tested the changes in activity of the Rho-GTPases RhoA, Rac1 and Cdc42 by performing pull-down assays of GTP-bound proteins from cell lysates. For Cdc42, we did not find obvious changes upon EMT in a cell population of mixed cell cycle stages (mainly interphase cells) or in isolated mitotic cells (Supplementary Figure S4). However, we observed a drastic increase of active Rac1 accompanied by a strong decrease of active RhoA upon EMT in both mitotic cells and a mixed cell population (Figure 4a,b). EMT-induced changes were more striking for a mixed cell population than for mitotic cells, indicating that RhoA was still activated post-EMT in mitosis.

### 2.4 Rac1 and RhoA activity cause a cell-cycle dependent cortex-mechanical switch

Since we observed a striking change in the activity of RhoA and Rac1 upon EMT, we asked how they respectively influenced the mechanical properties of the cortex. For this purpose, we performed a knock-down of RhoA or Rac1 by RNA interference in MCF-7 cells then performed cell-mechanical measurements in interphase and mitosis.

In interphase, cortical tension significantly increased after Rac1 knock-down, while the elastic modulus and phase shift did not show significant changes (Figure 4c-e, top row). By contrast, we observed a reduction of cortical tension and cortical stiffness as well as an increase in phase shift in mitotic cells. A decrease of mitotic cortical tension upon Rac1 knock-down was shown before<sup>39</sup>. We repeated this measurement for post-EMT cells and found that changes were qualitatively equal but stronger corresponding to above reported increased Rac1 activity in post-EMT conditions (Figure 4c-e, bottom row). In summary, Rac1 knockdown made the cortex more contractile in interphase and less contractile, less stiff and more liquid-like in mitosis. Therefore, Rac1 knock-down-induced changes are in all respects opposite to EMT-induced changes of cortical mechanics. Vice versa, we conclude that Rac1 activity increase triggers cell-mechanical changes that are qualitatively equal to EMT-induced changes (Figure 5d).

Knock-down of RhoA led to no significant mechanical changes of the cortex in interphase cells indicating that RhoA has, at best, a minor effect on cortical mechanics in non-adherent interphase cells (Figure 4f-h, top row). In mitosis, cortical stiffness and cortical tension decreased after RhoA knock-down as expected from previous work (Figure 4f-h, bottom row)<sup>6,7,12,39</sup>. The phase shift increase after RhoA knockdown indicates a fluidization of the cortex. Post-EMT, RhoA knockdown cells showed the same trend in cortex mechanical changes albeit less strongly, which is in accordance with our findings of EMT-induced reduction of RhoA activity.

In summary, both, Rac1 and RhoA signaling causes cortex-mechanical changes that depend qualitatively on the cell-cycle state of the cell (Figure 5d).

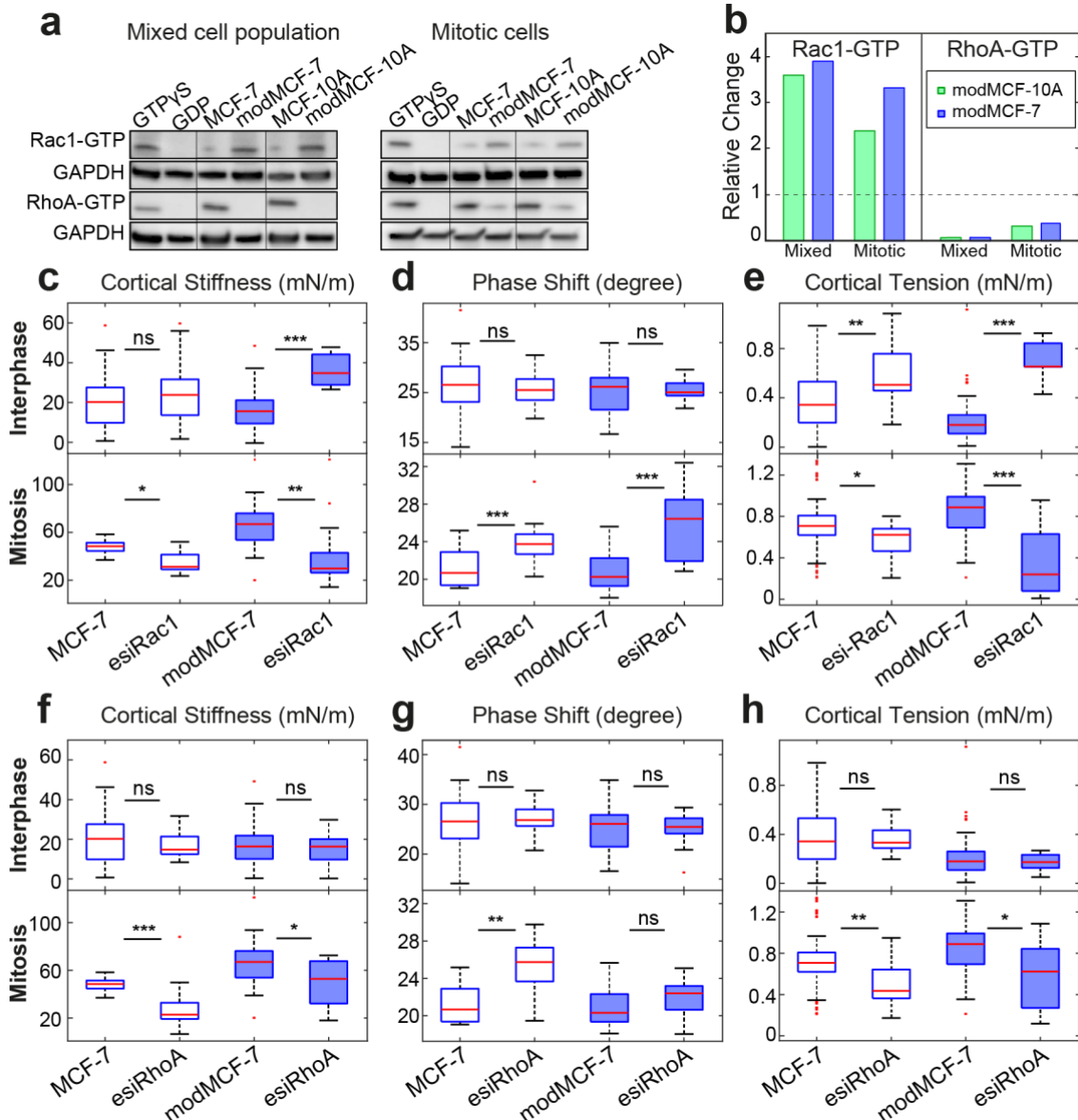


**Figure 4: Activity changes of Rac1 and RhoA upon EMT and related changes in cortical mechanics.** a,b) Rac1 and RhoA activity before and after EMT. a) Western blots showing GTP-bound Rac1 (top row) and RhoA (third row) before and after EMT. b) Quantification of western blot in a. c,d,e) Effect of Rac1 knock-down on cortex mechanics in MCF-7 and modMCF-7 (post-EMT) in suspended interphase MCF-7 cells (top row) and MCF-7 cells in mitotic arrest (bottom row). f,g,h) Effect of RhoA knock-down on cortex mechanics in MCF-7 and modMCF-7 (post-EMT) in suspended interphase MCF-7 cells (top row) and MCF-7 cells in mitotic arrest (bottom row). (Post-EMT cells are referred to as modMCF-7 and mod-MCF-10A, respectively. Number of cells measured: Interphase: MCF-7 n=24 and esiRac1 n=24, modMCF-7 n=10 and esiRac1 n=10, Mitosis: MCF-7 n=11 and esiRac1 n=12, modMCF-7 n=14 and esiRac1 n=14. Interphase: MCF-7 n=24 and esiRhoA n=17, modMCF-7 n=16 and esiRhoA n=13. Mitosis: MCF-7 n=11 and esiRhoA n=13, modMCF-7 n=14 and esiRhoA n=14. ns p>0.05, \*p < 0.05, \*\*p < 0.01, \*\*\*p < 0.001).

## 2.5 Down-stream effectors Limk1 and Arp2/3 can account for Rac1-induced mechanical changes of the cortex

We were interested to know which downstream effectors of Rac1 would give rise to a cell-cycle dependent cell-mechanical change. A good candidate was the Limk family of proteins, which has been shown to regulate actin dynamics by phosphorylating and inactivating cofilin, an actin-depolymerizing protein. Furthermore, Limk1 activity was previously reported to be enhanced during mitosis<sup>40</sup>. Consistent with this, we found that the mechanics of the interphase cortex of Limk1 knock-down cells did not change significantly upon Limk1 knock-down. By contrast, mitotic cortices of MCF-7 cells showed a significant reduction in stiffness and cortical tension and a substantial increase in phase shift (Figure 5a-c). Thus, the mitotic cortex becomes less contractile, less stiff and more liquid-like upon Limk1-knockdown.

Another major downstream effector of Rac1 is the Arp2/3 complex, which nucleates new branches of actin filaments and thus enhances actin polymerization. Surprisingly, we and others observed that inhibition of Arp2/3 by CK-666 (50  $\mu$ M) increased cortical tension in particular in interphase cells<sup>41</sup> (Figure 5c). In addition, our measurements showed an increase of phase shift upon Arp2/3 inhibition in interphase (Figure 5b). In mitosis, Arp2/3 inhibition increased cortical stiffness while the phase shift did not change significantly (Figure 5a,b).

Together, these findings suggest the following explanation of EMT-induced cell-mechanical changes: EMT increases Rac1 activity and thus the downstream activity of, both, Arp2/3 and Limk1 which have antagonistic effects on cortex mechanics; in interphase, the post-EMT cortex mechanical phenotype is dominated by an increased activity of Arp2/3 and largely unaffected by Limk1 activity increase; the mitotic post-EMT phenotype could then be explained by a stronger impact of Limk1 activity increase. Accordingly, we observed that inhibition of Arp2/3 jointly with Limk1 knock-down causes cortex-mechanical changes that can account for Rac1-knockdown-induced changes of cortical stiffness and contractility (Figure 5). The additional phase shift change in interphase cells upon Arp2/3 inhibition hints at an additional cortex effector downstream of Rac1 (Figure 5b).

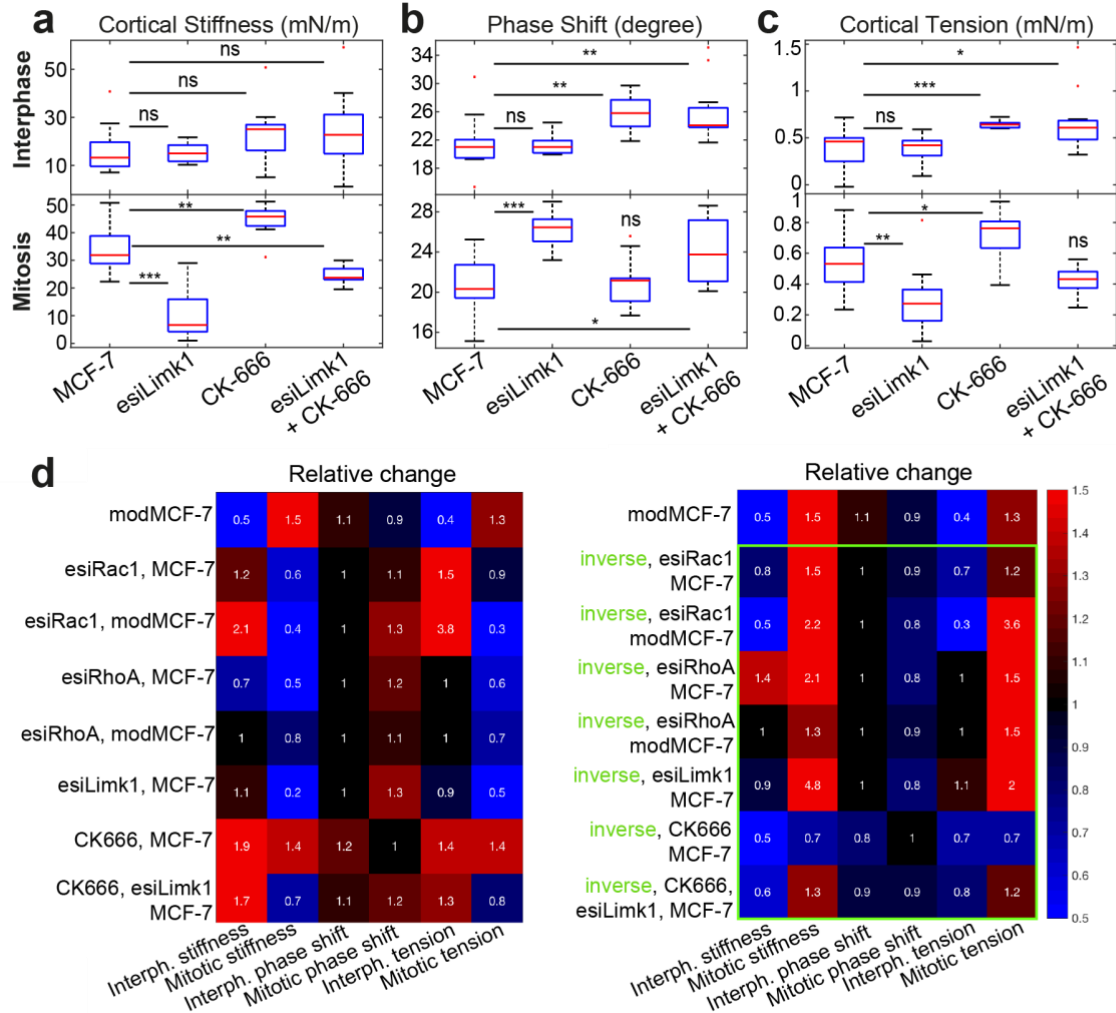


**Figure 5:** (a-c) Cortex mechanics before and after Limk1 knock-down and Arp2/3 inhibition through the cytoskeletal drug CK-666 (50  $\mu$ M) in suspended interphase MCF-7 (top row) and MCF-7 in mitotic arrest (bottom row). (Number of cells measured: Interphase: MCF-7 n=11, esiLIMK1 n=12, CK-666 n=12 and esiLIMK1 + CK-666 n=12, Mitosis: MCF-7 n=13, esiLIMK1 n=12, CK-666 n=11 and esiLIMK1 + CK-666 n=13). ( ns $p > 0.05$ , \* $p < 0.05$ , \*\* $p < 0.01$ , \*\*\* $p < 0.001$ ). d) Heat map showing relative changes of cortex mechanics in interphase and mitosis in MCF-7 cells for various conditions. Left panel, top to bottom: post-EMT, Rac1 knockdown, Rac1 knockdown post-EMT, RhoA knockdown, RhoA knockdown post-EMT, Limk1 knockdown, Arp2/3 inhibition via CK666 (50  $\mu$ M), Limk1 knockdown combined with Arp2/3 inhibition via CK666 (50  $\mu$ M). Relative changes are calculated as (median values of conditions)/(median values of control). Right panel: as in left panel but showing inverse numbers for second to last row, to depict the effect of protein activity increase.

## 2.6 Mitotic rounding in confined spheroids is enhanced through EMT

So far, we studied mitotic cells in 2D culture, where mitotic cells can easily become round since there are no mechanical obstacles to rounding. Accordingly, in 2D culture, mitotic cells are round in pre and post-EMT conditions. However, under physiologically relevant conditions, cells are mechanically confined by other cells or stroma. We therefore asked whether EMT and corresponding increase of cortical tension indeed lead to enhanced mitotic rounding when cells are cultured in a mechanically confining environments. To this end, we grew MCF-7 cells in 3D culture embedded in non-degradable PEG Heparin gel. Over time, cells grew into spheroidal cell aggregates which are mechanically confined by the gel. We quantified the roundness of MCF-7 cells in mitosis before and after EMT induction after seven days of growth (Figure 6a). 12-15 hours before fixation, S-trityl-L-cysteine (2  $\mu$ M) was added to arrest mitotic cells in mitosis in order to enrich mitotic cells. Spheroids were imaged through confocal z-stacks. For each mitotic cell, the largest cross-sectional area of the cell was used to quantify roundness (Figure 6b central panel, Materials and Methods). Furthermore, spheroid size was quantified by the largest cross-sectional area of the spheroid (Supplementary Figure S6). Increasing gel stiffness indeed reduces mitotic roundness and spheroid size most likely due to mechanical hindrance (Figure 6c). Furthermore, our data show an increase in mitotic roundness post-EMT and increased spheroid sizes (Figure 6c). In summary, these finding corroborate the idea that EMT induced cell-mechanical changes enhance mitotic rounding and, thus, promote cell proliferation in mechanically confining environment.

To identify whether cortical contractility contributed to this effect, we tested the effect of the myosin-inhibiting drug Blebbistatin on mitotic rounding in MCF-7 spheroids. Myosin inhibition reduces contractility in the actomyosin cytoskeleton. Indeed, we find that Blebbistatin reduces mitotic rounding in spheroids in pre- and post-EMT conditions (Figure 6d). These findings show evidence that actomyosin contractility has an influence on mitotic rounding and proliferation in 3D culture. However, an influence of altered cell adhesion may still not be ruled out entirely as actomyosin contractility has been shown to modify the lifetime and the architecture of focal adhesions and cell-cell contacts<sup>42</sup>.

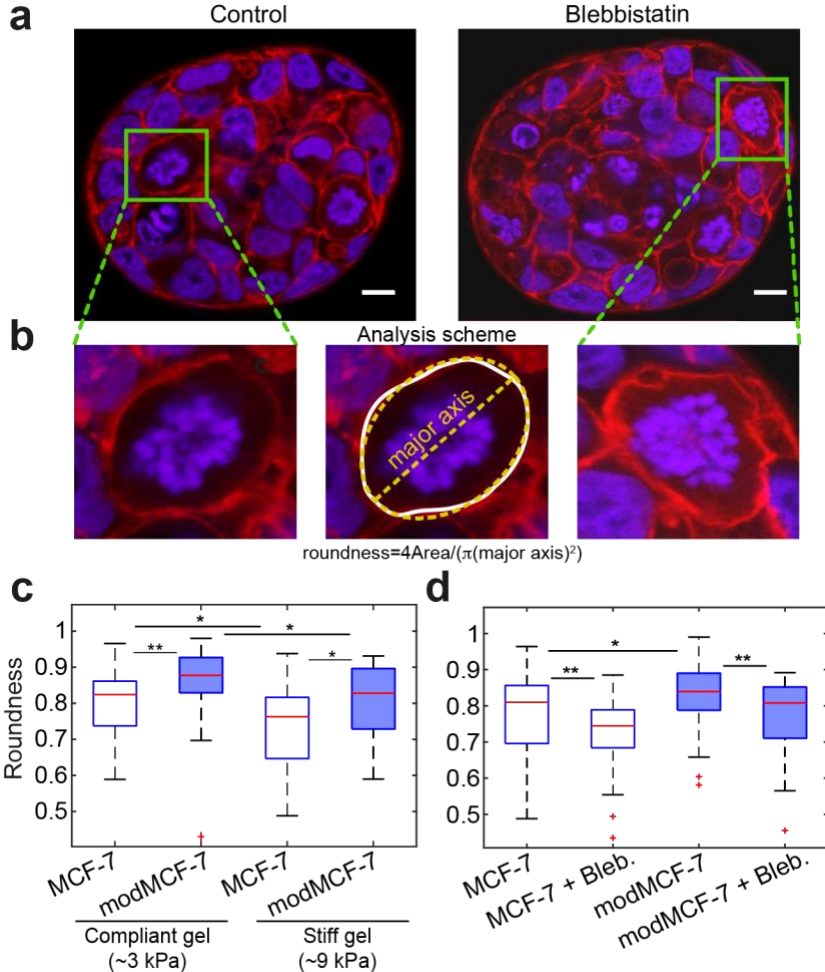


**Figure 6: The influence of EMT on mitotic roundness in MCF-7 tumor spheroids.** a) Confocal images of cross-sections of MCF-7 spheroids in PEG heparin gel. Cells were fixed and stained for DNA (DAPI, blue) and F-actin (phalloidin, red). Mitotic cells were arrested in mitosis through co-incubation with STC (2  $\mu\text{M}$ ) prior to fixation and exhibit condensed chromosomes (see e.g. cells in green frame). Left panel: control condition. Right panel: blebbistatin (10  $\mu\text{M}$ ) was added to the medium 2 hours prior to STC addition inhibiting myosin activity in cells. Scale bar: 10  $\mu\text{m}$ . b) Left and Right panel: zoom of cross-sections of mitotic cells in a. Center Panel: For image analysis, the cell outline of the largest cell cross-section was first determined (white). Roundness of the cell was then calculated using Fiji including the fit of an ellipse (yellow), see Materials and Methods. c) Roundness of mitotic cells in spheroids before and after EMT in compliant and stiff hydrogels (Young's modulus of ~3 or ~9 kPa, respectively). d) Roundness of mitotic cells in compliant gels with or without inhibition of cortical tension through the myosin inhibitor blebbistatin (10  $\mu\text{M}$ ). (Post-EMT cells are referred to as modMCF-7 and mod-MCF-10A, respectively. Number of mitotic cells analysed: Panel c: Compliant gel, MCF-7 n=94, modMCF-7 n=59, Stiff gel, MCF-7 n=31 and modMCF-7 n=40. Panel d: MCF-7 n=26, MCF-7+Bleb., n=54, modMCF-7 n=58 and modMCF-7+Bleb. n=47. ns $p>0.05$ , \* $p<0.05$ , \*\* $p<0.01$ , \*\*\* $p<0.001$ ).

### 3 Discussion

Here, we have shown that pharmacologically-induced EMT gives rise to a cell-cycle dependent switch in mechanical properties of the actin cell cortex of breast epithelial cells. In our study, we compared interphase cells in suspension and mitotic cells in 2D culture before and after EMT. In particular, we observed a softer, less contractile cortex in interphase cells and a more contractile, stiffer cortex phenotype in mitotic cells. Our observation that interphase post-EMT cells have a softer actin cytoskeleton is in agreement with a study by Osborne *et al.* that

reported softening of adherent cells upon EMT<sup>43</sup> and with reports that metastatic cancer cells are softer than healthy and non-metastatic cells<sup>20,44–46</sup>.

Enhanced cortical contractility of post-EMT breast epithelial cells in mitosis corresponds to an enhanced cell surface tension in mitosis and provides an important mechanical driving force for cell rounding<sup>1,3,5–11</sup>. Therefore, our findings suggest increased mitotic rounding strength for post-EMT breast epithelial cells and thus an increased potency to undergo successful mitotic rounding and cell division in mechanical confinement. Furthermore, our observation of concurrent softening of breast epithelial cells upon EMT may facilitate mitotic rounding further as post-EMT interphase cells in the neighborhood of a mitotic cell are more easily deformable. In fact, we could confirm enhanced mitotic rounding in post-EMT conditions by our observation of increased roundness of mitotic cells in spheroids growing in non-degradable Peg-Heparin hydrogels (Figure 6c,d). Furthermore, increased cross-sectional area of spheroids for post-EMT cells suggests a higher rate of successful cell divisions (Supplementary Figure S6).

In search of a molecular explanation for the altered cortex mechanics, we found that activity of the Rho GTPase Rac1 is strongly increased in MCF-7 and MCF-10A cells after EMT in accordance with previous findings<sup>47–51</sup>. By contrast, we found a strongly decreased activity of the Rho GTPase RhoA to be strongly decreased. This observation is consistent with the idea of a three-way switch operation of Rac1 and RhoA activation proposed by previous work<sup>47,52</sup>, in which the epithelial phenotype corresponds to a state with high levels of RhoA-GTP and low levels of Rac1-GTP while the mesenchymal state is characterized by the reversed trend.

Our cell-mechanical study indicates that EMT-induced mechanical changes of the cortex could be accounted for by the mechanical impact of EMT-induced Rac1 activation (Figure 7); we show that Rac1 activity decrease through gene knock-down induces cortex-mechanical changes that are opposite to EMT-induced changes in all six characterizing mechanical parameters (Figure 5d). Further, our data suggest that, downstream of Rac1, a combined increase of Arp2/3 and Limk1 activity can account for the observed changes of cortical stiffness and contractility upon EMT (Figure 5d).

In summary, we report here a cell-mechanical study that shows significant cell-cycle-dependent changes of cortex mechanics upon EMT that implies increased mitotic rounding strength of post-EMT breast epithelial cells (Figure 7). While EMT is commonly regarded to be connected to cancer progression through the promotion of cancer cell invasiveness, our findings indicate that EMT might also support cancer progression through enhanced mitotic cell rounding and preceding successful cell division in the increasingly crowded environment of a growing tumor.

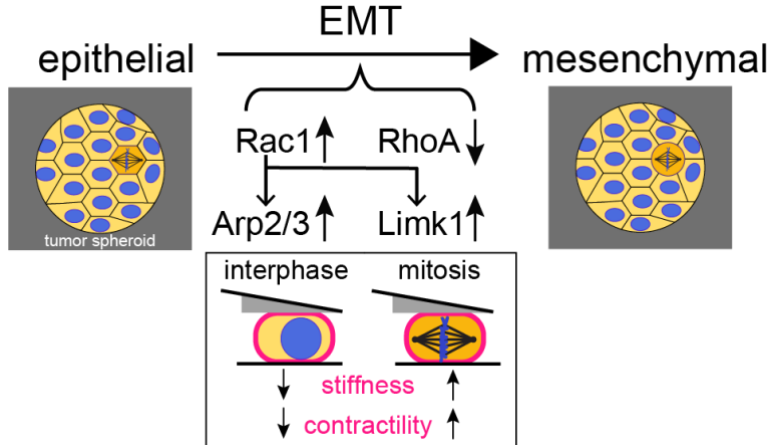


**Figure 7: Summary of our findings: EMT in breast epithelial cells MCF-7 and MCF-10A leads to cell-cycle-dependent cortex-mechanical changes: cortical stiffness and contractility are reduced in interphase cell but increased in mitotic cells. These findings suggest an increased rounding strength of post-EMT cells. In accordance with this, we observe increased roundness in mitotic cells in post-EMT MCF-7 spheroids. Cell-mechanical changes upon EMT are accompanied by a striking increase in Rac1 activity and decrease in RhoA activity. Rac1 signaling can account for EMT-induced cortex-mechanical changes via activation of downstream effectors Arp2/3 and Limk1.**

## 4 Materials and Methods

### 4.1 Cell culture

The cultured cells were maintained as follows: MCF-7 cells were grown in RPMI-1640 medium (PN:2187-034, life technologies) supplemented with 10% (v/v) fetal bovine serum, 100 µg/ml penicillin, 100 µg/ml streptomycin (all Invitrogen) at 37°C with 5% CO<sub>2</sub>. MCF-10A cells were cultured in DMEM/F12 medium (PN:11330-032, Invitrogen) supplemented with 5% (v/v) horse serum (PN:16050-122, Invitrogen), 100 µg/ml penicillin, 100 µg/ml streptomycin (all Invitrogen), 20 mg/ml epidermal growth factor (PN:AF-100-15, Peprotech), 0.5 mg/ml hydrocortisone (PN:H-0888, Sigma), 100 ng/ml cholera toxin (PN:C-8052, Sigma), 10 µg/ml insulin (PN:I-1882, Sigma) at 37°C with 5% CO<sub>2</sub>.

In MCF-7 cells, EMT was induced by incubating cells in medium supplemented with 100 nM 12-O-tetradecanoylphorbol-13-acetate (TPA) (PN:P8139, Sigma) for 48 hours prior to measurement<sup>26</sup>. In MCF-10A, EMT was induced by incubating cells in medium supplemented with 10 ng/ml TGF-β1 (PN:90900-1, BPSBioscience, San Diego, USA) one week prior to measurement<sup>27-29</sup>. Measured cell volumes before and after EMT induction are depicted in Supplementary Figure S3. For MCF-10A cells, we observe an average increase of cell volumes in mitosis of ~15%.

### 4.2 AFM measurements of cells

To prepare mitotic cells for AFM measurements, we seeded ~10.000 cells in a silicon cultivation chamber (0.56 cm<sup>2</sup> area, from ibidi 12-well chamber) that was placed in a 35 mm cell culture dish (fluorodish FD35-100, glass bottom, World Precision Instruments) one day before the measurement so that a confluence of approximately 30% was reached on the measurement day. We induced mitotic arrest by supplementing S-trityl-L-cysteine (STC, Sigma) 2-8 hours before the measurement at a concentration of 2 µM. For measurement, mitotically arrested cells were identified by their shape. Their uncompressed diameter ranged typically from 18-23 µm.

To prepare AFM measurements of suspended interphase cells, cell culture dishes (fluorodish FD35-100) were coated by incubating the dish at 37°C with 0.5 mg/ml PLL-g-PEG dissolved in PBS for 1 hour (SuSoS, Dubendorf, Switzerland) to prevent cell adhesion. Prior to

measurements, cultured cells were detached by the addition of 1X 0.05% trypsin-EDTA (Invitrogen). Approximately 30.000 cells in suspension were placed in the coated culture dish. The culture medium was changed to CO<sub>2</sub>-independent DMEM (RN: 12800-017, Invitrogen) with 4 mM NaHCO<sub>3</sub> buffered with 20 mM HEPES/NaOH pH 7.2, for AFM experiments approximately 2 hours before the measurement<sup>8,9,24</sup>.

The experimental set-up included an AFM (Nanowizard I, JPK Instruments) that was mounted on a Zeiss Axiovert 200M optical, wide-field microscope. 20x objective (Zeiss, Plan Apochromat, NA=0.8) along with a CCD camera (DMK 23U445 from Theimagingsource). Cell culture dishes were kept in a petri dish heater (JPK Instruments) at 37°C during the experiment. Prior to every experiment, the spring constant of the cantilever was calibrated by thermal noise analysis (built-in software, JPK) using a correction factor of 0.817 for rectangular cantilevers<sup>53</sup>. The cantilevers used were tipless, 200 – 350 μm long, 35 μm wide and 2 μm thick (NSC12/tipless/no Aluminium or CSC37/tipless/no Aluminium, Mikromasch). The nominal force constants of the cantilevers ranged between 0.2 – 0.8 N/m. The cantilevers were supplied with a wedge, consisting of UV curing adhesive (Norland 63, Norland Products Inc.) to correct for the 10° tilt<sup>54</sup>. The measured force, piezo height and time were output at a time resolution of 500 Hz.

**Oscillatory cell compression protocol:** Preceding every cell compression, the AFM cantilever was lowered to the dish bottom in the vicinity of the cell until it touched the surface and then retracted to approximately 15 μm above the surface. Subsequently, the free cantilever was moved and placed on top of the cell. Thereupon, a bright-field image of the equatorial plane of the confined cell is recorded in order to evaluate the equatorial cross-sectional area at a defined cell height, which in turn is used to estimate the cell volume as described in earlier work<sup>24</sup>. As the cell is sandwiched between the dish bottom and cantilever wedge, oscillatory height modulations of the AFM cantilever were undertaken, with piezo oscillation amplitudes of 0.25 μm at a frequency of 1 Hz if not indicated otherwise. Throughout this step, the cell was typically maintained at a height corresponding to 60-70% of the expected cell height if the cell were a perfect sphere at equal volume. Oscillatory cantilever height modulations were produced by a piecewise linear approximation of the sine-function<sup>24</sup>. The force acting on the cantilever and the height of the cantilever was constantly recorded. The height of the confined cell was calculated as the difference between the height that the cantilever was elevated above the dish surface and lowered onto the cell with the addition of the spike heights at the boundary of the wedge (formed by imperfections during the manufacturing process<sup>54</sup>) and the force-induced deflection of the cantilever. We estimate a total error of the cell height of approximately 0.5 μm due to irregularities of the cantilever wedge and vertical movement of the cantilever to a position above the cell.

**Data analysis of AFM measurements:** The data analysis procedure has been described in detail in earlier work<sup>24</sup>. In brief, the time series of measured AFM force  $F$  and AFM cantilever height  $h$  were analyzed in the following way: Data analysis of oscillatory measurements were performed after a transient relaxation phase in a time interval of steady state oscillations (constant force and constant cantilever height oscillation amplitude, see Figure 3). In an analysis time window of 5-10 periods, we estimated for every time point effective tension  $\gamma_{eff} = F_{AFM}/A_{con}(1/R_1 + 1/R_2)$  and relative cell surface area change (area strain)  $\epsilon_A = (A - \langle A \rangle)/\langle A \rangle$ . Here  $R_1, R_2$  and  $A_{con}$  denote geometrical parameters of cell shape (radii of curvature and contact area), while  $A$  indicates the cell surface area and  $\langle A \rangle$  denotes its time-averaged value. Geometrical parameters of cell shape are calculated assuming a shape of minimal surface area at constant cell volume as described before<sup>34</sup>. Cortical tension  $\gamma$  was estimated as the time-averaged value of  $\gamma_{eff}$  during an oscillation period.

For a rheological analysis, effective cortical tension  $\gamma_{eff}$  is interpreted as stress readout, while  $\epsilon_A$  is interpreted as strain readout. An amplitude and a phase angle associated to the oscillatory time variation of stress and strain are extracted. To estimate the value of the complex elastic

modulus at a distinct frequency, we determine the phase angles  $\varphi_Y$  and  $\varphi_{\epsilon_A}$  as well as amplitudes  $\hat{\gamma}_{eff}$  and  $\hat{\epsilon}_A$  of effective tension and surface area strain, respectively. Cortical stiffness was calculated as  $\hat{\gamma}_{eff}/\hat{\epsilon}_A$  while the phase shift was determined as  $\varphi = (\varphi_Y - \varphi_A)$ . Statistical analysis of cortex mechanical parameters was performed in Matlab using the commands ‘boxplot’ and ‘ranksum’ to generate boxplots and determine p-values from a Mann-Whitney U-test, respectively.

#### 4.3 Western blotting

Protein expression in MCF-10A and MCF-7 before and after EMT was analysed using western blotting. Cells were seeded onto a 6-well plate and grown up to a confluence of 80–90% with or without EMT-inducing agents. Thereafter, cells were lysed in SDS sample/lysis buffer (62.5 mM TrisHCl pH 6.8, 2% SDS, 10% Glycerol, 50 mM DTT and 0.01% Bromophenolblue). The cells lysates were run on precast protein gels (PN:456-1096 or 456-1093, Bio-Rad) in MOPS SDS running buffer (B0001, Invitrogen). Subsequently, proteins were transferred to PVDF membranes (Millipore). PVDF membranes were blocked with 5% (w/v) skimmed milk powder (T145.1, Carl Roth, Karlsruhe, Germany) in TBST (20 mM/L Tris-HCl, 137 mM/L NaCl, 0.1% Tween 20 (pH 7.6)) for 1 h at room temperature followed by washing with TBST, and incubation at 4°C overnight with the corresponding primary antibody diluted in 1:1000 (Vimentin, E-Cadherin, N-Cadherin, Rac1) or 1:500 (RhoA, Cdc42) or 1:5000 (GAPDH) 3% (w/v) bovine serum albumin/TBST solution. Thereupon, the blots were incubated with appropriate secondary antibodies conjugated to horseradish peroxidase, Rabbit anti-mouse HRP (PN:ab97045, Abcam) or Goat anti-rabbit HRP (PN:ab97051, Abcam) at 1:3000 dilution in 5% (w/v) skimmed milk powder in TBST for 1 h at room temperature. After TBST washings, specifically bound antibodies were detected using Pierce enhanced chemiluminescence substrate (ECL) (PN:32109, Invitrogen). The bands were visualised and analysed using a CCD-based digital blot scanner, ImageQuant LAS4000 (GE Healthcare Europe, Freiburg, Germany). Primary antibodies used are as follows: E-Cadherin (PN:5296, Cell Signalling Technology), Vimentin (PN:AMF-17b, DSHB Technologies), N-Cadherin (PN:13116, Cell Signalling Technologies), GAPDH (PN:ab9485, Abcam), RhoA (PN:ARH04, Cytoskeleton Inc.), Cdc42 (PN:ACD03, Cytoskeleton Inc.) and Rac1 (PN:PA1091X, Invitrogen).

P-values of western blots were determined with Mathematica using a univariate t-test testing the hypothesis that the distribution of relative changes in control conditions is either larger or smaller than one.

#### 4.4 Active Rho-GTPase pull-down assay

Pull-down assays were performed for RhoA-GTP, Rac1-GTP and Cdc42-GTP using the RhoA and Cdc42 pull-down activation assay biochem kit (PN:BK036-S and BK034-S, Cytoskeleton, Inc.) following the protocol provided by the manufacturer. Briefly, cells were lysed in lysis buffer and supplemented with 1 mM Protease Inhibitor Cocktail. Cell lysates were harvested rapidly on ice with a cell scraper. The mitotic cells were collected by shake-off. The lysates were then centrifuged at 15,000 rpm for 5 min at 4°C. 20–50 µg lysate was used for western blot. Equivalent lysate protein amounts (500 µg total cell protein) were added to a pre-determined amount of rhokin-RBD beads at 4°C. Beads were incubated for 60 min with gentle rocking, before collecting them by centrifugation at 15,000 rpm for 1 min at 4°C. After being washed in washing buffer, beads were resuspended in 20 µl of SDS sample/lysis buffer (described in section 4.3), then boiled for 2 min. The supernatant was then analysed by SDS-PAGE and western blot as described in the previous section. Cell lysate mixed with non-hydrolysable GTPγS or GDP were used as a positive and negative control, respectively, according to the protocol of the manufacturer.

#### 4.5 Gene knock-down through RNA interference

We performed gene knock-downs through RNA interference (RNAi). Cells were transfected with primary esiRNA (Eupheria Biotech, Dresden, Germany) targeting the genes Rac1, RhoA and Limk1 at a concentration of 25 nM, using the transfection reagent Lipofectamin RNAiMax (Invitrogen). For a negative control, we used firefly luciferase esiRNA (F-Luc). For a positive control, we used Eg5/kif11 esiRNA, which in all cases resulted in mitotic arrest of more than 60% of the cells (indicating a transfection efficiency of more than 60% for each experiment). At day 0, 30,000 cells were seeded into a 24-well plate (NuncMicroWell Plates with Nunclon; Thermo Fisher Scientific, Waltham, MA). Transfection was carried out at day 1, medium was exchanged at day 2 (without antibiotics) (day 3 for Limk1), and transfected cells were measured at day 3 (day 4 for Limk1). For mitotic cells, approximately 12 hours before measurements, cells were detached, diluted, and transferred onto a glass-bottom petri dish (FD35-100, World Precision Instruments) to obtain a confluence of 20 – 40% during AFM measurements. For interphase cells, 2-3 hours before measurement the cells were detached and transferred to PLL-g-PEG-coated petri dishes (see Section on AFM measurements of cells).

Measured cell volumes before and after gene knock-downs are depicted in Supplementary Figures S4 and S5, respectively. Our data indicate a decrease in cell volume upon Rac1 knock-down pre-EMT in mitotic cells and a reduction in interphase cell volume for post-EMT conditions (Supplementary Figure S4c). RhoA and Limk1 knock-down did not elicit any significant cell volume changes (Supplementary Figure S4c and S5).

#### 4.6 Preparation of spheroids in starPEG-Heparin hydrogels

*In situ* assembling biohybrid multiarmed poly(ethylene glycol) (starPEG)-heparin hydrogels, prepared as previously reported<sup>55</sup>, were used for embedding cells to grow into spheroids. In brief, cells were detached from the tissue flasks and resuspended in PBS. Subsequently, they were mixed with freshly prepared heparin-maleimide-8 solution at a density of approximately  $5 \times 10^5$  cells/ml, and a final heparin-maleimide concentration of 3 mM<sup>25</sup>. PEG precursors were reconstituted at a concentration of 3 mM and put in an ultrasonic bath for 10-20s in order to dissolve. We then mixed 15  $\mu$ l of the heparin-cell suspension with equal volume of PEG solution in a pre-chilled Eppendorf tube, using a low binding pipette tip. Thereafter, a 25  $\mu$ l drop of PEG-heparin-cell mixture was pipetted onto a hydrophobic glass slide. After gelling, hydrogels were gently detached from the glass slide and placed in a 24-well plate supplemented with the cell culture medium. The spheroids were allowed to grow in the non-degradable hydrogel constructs for 7 days including the chemical treatment time for EMT-induction, before being fixed and immunostained. Medium was exchanged every second day. The medium was supplemented with 1  $\mu$ M STC to enrich mitotic cells 13-15 h prior to fixation. Where indicated, Blebbistatin was added to a concentration of 10  $\mu$ M two hours prior to addition of STC.

#### 4.7 Quantification of hydrogel stiffness

Disc-shaped hydrogels, not seeded with cells, were immersed in PBS after preparation and kept at 4 °C to the following day for mechanical quantification. After equilibrating them at room temperature for 1 hour, gels were mounted onto glass object slides using Cell-Tak™ (Thermofisher). Gel stiffness was probed by AFM indentation<sup>18,56,57</sup>. Cantilevers (arrow T1, Nanoworld), that had been modified with polystyrene beads of 10  $\mu$ m diameter (Microparticles GmbH) using epoxy glue (Araldite), were calibrated using the thermal noise method implemented in the AFM software and probed at room temperature in PBS using a speed of 5  $\mu$ m/sec and a relative force setpoint of 2.5 nN. Force distance curves were processed using the JPK data processing software. Indentation parts of the force curves (about 1  $\mu$ m depth) were fitted using the Hertz model for a spherical indenter, assuming a Poisson ratio of 0.5.

#### 4.8 Immunostaining and confocal imaging of spheroids in hydrogel constructs

The tumour spheroid hydrogel constructs were fixed at day 7 with 4% formaldehyde/PBS for 1 h, followed by a 30 min permeabilization step in 0.2% Triton X-100. The spheroids were then stained for 4 h with 5 µg/ml DAPI and 0.2µg/ml Phalloidin-Alexa Fluor 488 in 2% BSA/PBS solution. Then hydrogels were immersed at least for 1 hour in PBS. For imaging, hydrogels were cut horizontally with a blade and were placed on a cover slip to image the interior of the hydrogel. Per hydrogel 5-15 spheroids were imaged recording a confocal z-stack with a Zeiss LSM700 confocal microscope of the CMCB light microscopy facility, using a Zeiss C-Apochromat 40x/1.2 water objective (z-step: 0.4-0.9 µm).

#### 4.9 Image analysis of spheroid confocal images

The software Fiji was used to characterize morphology of mitotic cells inside spheroids. We identified mitotic cells inside a spheroid from spheroid z-stacks (red channel, F-actin, blue channel, DNA) by observing DNA structure. The largest cross-sectional area in the z-stack of each mitotic cell was determined manually by actin fluorescence, which was then used to calculate the cross-sectional shape factor roundness. Roundness is determined using Fiji by fitting an ellipse to the cross-section and calculating  $4(Area)/(\pi(major\ axis)^2)$ , where *Area* is the cross-sectional area. Furthermore, spheroid size was quantified by the largest cross-sectional area of the spheroid (Supplementary Figure S6).

Statistical analysis of mitotic cell roundness in different conditions was performed in Matlab using the commands ‘boxplot’ and ‘ranksum’ to generate boxplots and determine p-values from a Mann-Whitney U-test, respectively.

### 5 Acknowledgements

We thank Mark Leaver, Carsten Hoege and Benjamin Friedrich for critical reading of the manuscript and helpful comments and Alf Honigmann and Stephan Grill for fruitful discussions on the project. Furthermore, we thank Jochen Guck and Isabel Richter for access and introduction to infrastructure in the lab. In addition, we thank the CMCB light microscopy facility for excellent support.

### Bibliography

1. Théry, M. & Bornens, M. Get round and stiff for mitosis. *HFSP J.* **2**, 65–71 (2008).
2. Lancaster, O. M. *et al.* Mitotic Rounding Alters Cell Geometry to Ensure Efficient Bipolar Spindle Formation. *Dev. Cell* **25**, 270–283 (2013).
3. Hoijman, E., Rubbini, D., Colombelli, J. & Alsina, B. Mitotic cell rounding and epithelial thinning regulate lumen growth and shape. *Nat. Commun.* **6**, 7355 (2015).
4. Straight, A. F. *et al.* Dissecting Temporal and Spatial Control of Cytokinesis with a Myosin II Inhibitor. *Science* **299**, 1743–1747 (2003).
5. Chanet, S., Sharan, R., Khan, Z. & Martin, A. C. Myosin 2-Induced Mitotic Rounding Enables Columnar Epithelial Cells to Interpret Cortical Spindle Positioning Cues. *Curr. Biol.* **27**, 3350-3358.e3 (2017).
6. Ramanathan, S. P. *et al.* Cdk1-dependent mitotic enrichment of cortical myosin II promotes cell rounding against confinement. *Nat. Cell Biol.* **17**, 148–159 (2015).
7. Matthews, H. K. *et al.* Changes in Ect2 localization couple actomyosin-dependent cell shape changes to mitotic progression. *Dev. Cell* **23**, 371–383 (2012).
8. Stewart, M. P. *et al.* Hydrostatic pressure and the actomyosin cortex drive mitotic cell rounding. *Nature* **469**, 226–230 (2011).
9. Fischer-Friedrich, E., Hyman, A. A., Jülicher, F., Müller, D. J. & Helenius, J. Quantification of surface tension and internal pressure generated by single mitotic cells. *Sci. Rep.* **4**, (2014).

10. Rosa, A., Vlassaks, E., Pichaud, F. & Baum, B. Ect2/Pbl Acts via Rho and Polarity Proteins to Direct the Assembly of an Isotropic Actomyosin Cortex upon Mitotic Entry. *Dev. Cell* **32**, 604–616 (2015).
11. Sorce, B. *et al.* Mitotic cells contract actomyosin cortex and generate pressure to round against or escape epithelial confinement. *Nat. Commun.* **6**, 8872 (2015).
12. Maddox, A. S. & Burridge, K. RhoA is required for cortical retraction and rigidity during mitotic cell rounding. *J. Cell Biol.* **160**, 255–265 (2003).
13. Heng, Y.-W. & Koh, C.-G. Actin cytoskeleton dynamics and the cell division cycle. *Int. J. Biochem. Cell Biol.* **42**, 1622–1633 (2010).
14. Jain, R. K., Martin, J. D. & Stylianopoulos, T. The Role of Mechanical Forces in Tumor Growth and Therapy. *Annu. Rev. Biomed. Eng.* **16**, 321–346 (2014).
15. Helmlinger, G., Netti, P. A., Lichtenbeld, H. C., Melder, R. J. & Jain, R. K. Solid stress inhibits the growth of multicellular tumor spheroids. *Nat. Biotechnol.* **15**, 778–783 (1997).
16. Montel, F. *et al.* Stress Clamp Experiments on Multicellular Tumor Spheroids. *Phys. Rev. Lett.* **107**, 188102 (2011).
17. Monnier, S. *et al.* Effect of an osmotic stress on multicellular aggregates. *Methods* **94**, 114–119 (2016).
18. Taubenberger, A. V. *et al.* 3D microenvironment stiffness regulates tumor spheroid growth and mechanics via p21 and ROCK. *bioRxiv* 586784 (2019). doi:10.1101/586784
19. Matthews, H. K. & Baum, B. The metastatic cancer cell cortex: An adaptation to enhance robust cell division in novel environments? *BioEssays* **34**, 1017–1020 (2012).
20. Matthews, H. K. *et al.* Oncogenic signaling alters cell shape and mechanics to facilitate cell division under confinement. *bioRxiv* 571885 (2019). doi:10.1101/571885
21. Scheel, C. & Weinberg, R. A. Cancer stem cells and epithelial–mesenchymal transition: Concepts and molecular links. *Semin. Cancer Biol.* **22**, 396–403 (2012).
22. Dongre, A. & Weinberg, R. A. New insights into the mechanisms of epithelial–mesenchymal transition and implications for cancer. *Nat. Rev. Mol. Cell Biol.* **1** (2018). doi:10.1038/s41580-018-0080-4
23. Felipe Lima, J., Nofech-Mozes, S., Bayani, J. & Bartlett, J. M. S. EMT in Breast Carcinoma—A Review. *J. Clin. Med.* **5**, (2016).
24. Fischer-Friedrich, E. *et al.* Rheology of the Active Cell Cortex in Mitosis. *Biophys. J.* **111**, 589–600 (2016).
25. M. V. Tsurkan, M., R. Levental, K., Freudenberg, U. & Werner, C. Enzymatically degradable heparin -polyethylene glycol gels with controlled mechanical properties. *Chem. Commun.* **46**, 1141–1143 (2010).
26. Kamiya, T., Goto, A., Kurokawa, E., Hara, H. & Adachi, T. Cross Talk Mechanism among EMT, ROS, and Histone Acetylation in Phorbol Ester-Treated Human Breast Cancer MCF-7 Cells. *Oxid. Med. Cell. Longev.* **2016**, 1–11 (2016).
27. Zhang, J. *et al.* TGF- $\beta$ -induced epithelial-to-mesenchymal transition proceeds through stepwise activation of multiple feedback loops. *Sci. Signal.* **7**, ra91 (2014).
28. Xu, J., Lamouille, S. & Derynck, R. TGF- $\beta$ -induced epithelial to mesenchymal transition. *Cell Res.* **19**, 156–172 (2009).
29. Liang, Q. *et al.* CDK5 is essential for TGF- $\beta$ 1-induced epithelial-mesenchymal transition and breast cancer progression. *Sci. Rep.* **3**, 2932 (2013).
30. Seton-Rogers, S. E. *et al.* Cooperation of the ErbB2 receptor and transforming growth factor  $\beta$  in induction of migration and invasion in mammary epithelial cells. *Proc. Natl. Acad. Sci.* **101**, 1257–1262 (2004).

31. Chen, C.-R., Kang, Y. & Massagué, J. Defective repression of c-myc in breast cancer cells: A loss at the core of the transforming growth factor  $\beta$  growth arrest program. *Proc. Natl. Acad. Sci.* **98**, 992–999 (2001).
32. Stewart, M. P. et al. Wedged AFM-cantilevers for parallel plate cell mechanics. *Methods* **60**, 186–194 (2013).
33. Fischer-Friedrich, E., Hyman, A. A., Jülicher, F., Müller, D. J. & Helenius, J. Quantification of surface tension and internal pressure generated by single mitotic cells. *Sci. Rep.* **4**, (2015).
34. Fischer-Friedrich, E. et al. Rheology of the Active Cell Cortex in Mitosis. *Biophys. J.* **111**, 589–600 (2016).
35. Stewart, M. P. et al. Hydrostatic pressure and the actomyosin cortex drive mitotic cell rounding. *Nature* **469**, 226–230 (2011).
36. Zhou, K. et al. RAC1-GTP promotes epithelial-mesenchymal transition and invasion of colorectal cancer by activation of STAT3. *Lab. Investig. J. Tech. Methods Pathol.* **98**, 989–998 (2018).
37. Santibáñez, J. F., Kocić, J., Fabra, A., Cano, A. & Quintanilla, M. Rac1 modulates TGF- $\beta$ 1-mediated epithelial cell plasticity and MMP9 production in transformed keratinocytes. *FEBS Lett.* **584**, 2305–2310 (2010).
38. Bellovin, D. I., Bates, R. C., Muzikansky, A., Rimm, D. L. & Mercurio, A. M. Altered localization of p120 catenin during epithelial to mesenchymal transition of colon carcinoma is prognostic for aggressive disease. *Cancer Res.* **65**, 10938–10945 (2005).
39. Toyoda, Y. et al. Genome-scale single-cell mechanical phenotyping reveals disease-related genes involved in mitotic rounding. *Nat. Commun.* **8**, (2017).
40. Kaji, N., Muramoto, A. & Mizuno, K. LIM kinase-mediated cofilin phosphorylation during mitosis is required for precise spindle positioning. *J. Biol. Chem.* **283**, 4983–4992 (2008).
41. Cartagena-Rivera, A. X., Logue, J. S., Waterman, C. M. & Chadwick, R. S. Actomyosin Cortical Mechanical Properties in Nonadherent Cells Determined by Atomic Force Microscopy. *Biophys. J.* **110**, 2528–2539 (2016).
42. Iskratsch, T., Wolfenson, H. & Sheetz, M. P. Appreciating force and shape — the rise of mechanotransduction in cell biology. *Nat. Rev. Mol. Cell Biol.* **15**, 825–833 (2014).
43. Osborne, L. D. et al. TGF- $\beta$  regulates LARG and GEF-H1 during EMT to affect stiffening response to force and cell invasion. *Mol. Biol. Cell* **25**, 3528–3540 (2014).
44. Alibert, C., Goud, B. & Manneville, J.-B. Are cancer cells really softer than normal cells? *Biol. Cell* **109**, 167–189 (2017).
45. Lin, H.-H. et al. Mechanical phenotype of cancer cells: cell softening and loss of stiffness sensing. *Oncotarget* **6**, 20946–20958 (2015).
46. Guck, J. et al. Optical Deformability as an Inherent Cell Marker for Testing Malignant Transformation and Metastatic Competence. *Biophys. J.* **88**, 3689–3698 (2005).
47. Huang, B. et al. The three-way switch operation of Rac1/RhoA GTPase-based circuit controlling amoeboid-hybrid-mesenchymal transition. *Sci. Rep.* **4**, 6449 (2014).
48. Zhou, Y. et al. Rac1 overexpression is correlated with epithelial mesenchymal transition and predicts poor prognosis in non-small cell lung cancer. *J. Cancer* **7**, 2100–2109 (2016).
49. Zhou, K. et al. RAC1-GTP promotes epithelial-mesenchymal transition and invasion of colorectal cancer by activation of STAT3. *Lab. Investig. J. Tech. Methods Pathol.* **98**, 989–998 (2018).
50. Akunuru, S., James Zhai, Q. & Zheng, Y. Non-small cell lung cancer stem/progenitor cells are enriched in multiple distinct phenotypic subpopulations and exhibit plasticity. *Cell Death Dis.* **3**, e352 (2012).

51. Justilien, V. & Fields, A. P. Ect2 links the PKC $\zeta$ –Par6 $\alpha$  complex to Rac1 activation and cellular transformation. *Oncogene* **28**, 3597–3607 (2009).
52. Byrne, K. M. *et al.* Bistability in the Rac1, PAK, and RhoA Signaling Network Drives Actin Cytoskeleton Dynamics and Cell Motility Switches. *Cell Syst.* **2**, 38–48 (2016).
53. Butt, H.-J. & Jaschke, M. Calculation of thermal noise in atomic force microscopy. *Nanotechnology* **6**, 1–7 (1995).
54. Stewart, M. P. *et al.* Wedged AFM-cantilevers for parallel plate cell mechanics. *Methods* **60**, 186–194 (2013).
55. Tsurkan, M. V. *et al.* Defined Polymer–Peptide Conjugates to Form Cell-Instructive starPEG–Heparin Matrices In Situ. *Adv. Mater.* **25**, 2606–2610 (2013).
56. Bray, L. J. *et al.* Multi-parametric hydrogels support 3D in vitro bioengineered microenvironment models of tumour angiogenesis. *Biomaterials* **53**, 609–620 (2015).
57. Papadimitriou, C. *et al.* Instructive starPEG-Heparin biohybrid 3D cultures for modeling human neural stem cell plasticity, neurogenesis, and neurodegeneration. *bioRxiv* 225243 (2017). doi:10.1101/225243